JOURNAL OF AIRCRAFT
Vol. 46, No. 5, September–October 2009

Elastic Multibody Models of Transport Aircraft High-Lift Mechanisms

János Zierath* and Christoph Woernle†
University of Rostock, 18051 Rostock, Germany
and
Thomas Heyden‡
Airbus Deutschland, GmbH, 28199 Bremen, Germany,

DOI: 10.2514/1.37583

In development of transport aircraft high-lift systems, the application of commercial simulation tools is widely used. This paper provides a short overview of parametric modeling of the mechanisms of the high-lift system of a transport aircraft as an elastic multibody system. Elastic mechanical components are modeled by means of the method of finite elements. The high-lift mechanisms comprise the leading-edge devices (droop nose, slats) and the trailing-edge devices (flaps). After giving some details of the theoretical background of elastic multibody systems, the specific models of the high-lift mechanisms are described. Simulation results of representative parameter studies demonstrate the application of the model. Some failure cases are also investigated in addition to an operating load case.

Nomenclature

$\mathbf{D}$ = deformation tensor
F = force
$\mathbf{F}$ = load vector
$\mathbf{f}$ = modal load vector
$\mathbf{G}$ = constraint matrix
$\mathbf{g}$ = residuals of implicit constraints
$\mathbf{K}$ = stiffness matrix
$\mathbf{M}$ = mass matrix
$\mathbf{N}$ = modal matrix
$\mathbf{q}$ = modal coordinates
$\bar{\mathbf{q}}$ = eigenvector
$\mathbf{q}^*$ = Craig–Bampton coordinates
$\mathbf{r}$ = position vector
$\mathbf{u}$ = physical displacement vector
$\mathbf{v}$ = velocity vector
$\boldsymbol{\gamma}$ = Euler angles
$\boldsymbol{\varepsilon}$ = strain vector
λ = eigenvalue
$\boldsymbol{\lambda}$ = reaction force coordinates
$\boldsymbol{\sigma}$ = stress vector
$\boldsymbol{\Phi}$ = modal matrix
$\boldsymbol{\omega}$ = angular velocity vector

I. Introduction

ONGOING aircraft developments in the fields of aerodynamics, structures, and engines had led to continuously increasing aircraft cruise speeds until the end of the 1960s. However, the takeoff/landing speed has not increased in the same ratio because of runway length limitations and landing gear and tire loading capacity restrictions. As a consequence, the aircraft speed ratio between cruise and takeoff/landing has increased from about two to three in modern transport aircraft.

This necessitates a variation of the lift coefficient to provide sufficient lift for takeoff and landing at lower speeds. Aircraft lift coefficient is varied by increasing wing area and wing curvature by the use of so-called high-lift systems. These systems typically comprise of movable devices, at the wing's leading edge (slats and droop nose) and the wing's trailing edge (flaps), that are spatially guided by mechanisms, as shown in Fig. 1.

In cruise configuration, high-lift devices blend into the main wing in order to minimize drag (Fig. 2). In takeoff/landing conditions, the wing area and curvature are increased by extending the flaps and slats. Additional information about high-lift systems and the different types used for commercial aircraft are found in [1–4].

High-lift design is a multidisciplinary process affecting overall wing design. As a result of aerodynamic predesign, the aerodynamic layout of the high-lift devices and their takeoff/landing settings are specified, and preliminary airloads are calculated. In the subsequent system development phase, the high-lift guidance and drive mechanisms are defined. In parallel, high-lift structures (i.e., flaps, slats, and support structure) are developed. Afterward, the high-lift design concept is analyzed and evaluated with respect to weight, costs, complexity, and maintainability. Several iterations may be necessary to find the optimum design solution.

The predevelopment phase is strongly supported by simulation, whereby the modeling approach depends on the specific design topic. In the field of aerodynamics, computational fluid dynamic techniques are used. Detailed structure development is based on static finite element (FE) analysis. Furthermore, the dynamics of the high-lift mechanisms have to be taken into account. For this purpose, the multibody model approach is well suited as it describes the large rigid-body motions of the mechanisms. A model with a low degree-of-freedom (DOF) number is obtained that is suitable for dynamic evaluation.

This paper describes multibody modeling of high-lift mechanisms of transport aircraft using the multibody simulation environment software MSC.Adams; however, other multibody simulation environments could be used as well. Highly stiff components (i.e., tension struts) are modeled as rigid bodies. Bodies subjected to larger deflections, like flaps, slats, or lever arms, are modeled as linear-elastic bodies that are integrated into the multibody model. Altogether, a hybrid model is obtained that couples large rigid-body motions with small flexible-body deformations. It is suitable for the

---

Received 17 March 2008; revision received 23 March 2009; accepted for publication 24 March 2009.

*Graduate Researcher, Department of Mechanical Engineering; janos.zierath@uni-rostock.de.

†Professor, Department of Mechanical Engineering; woernle@uni-rostock.de.

‡High-Lift System Engineering Department; thomas.heyden@airbus.com.

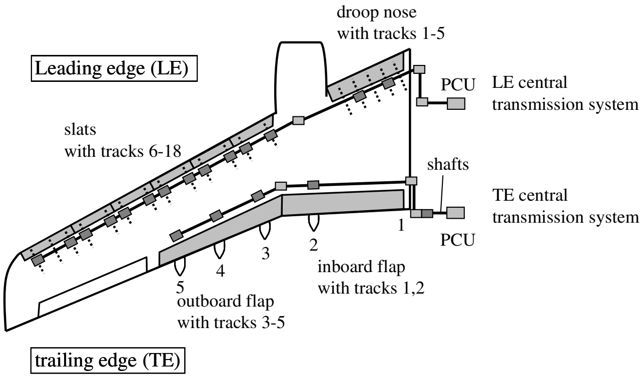

Fig. 1 Wing with leading-edge devices (slats and droop nose) and trailing-edge devices (flaps).

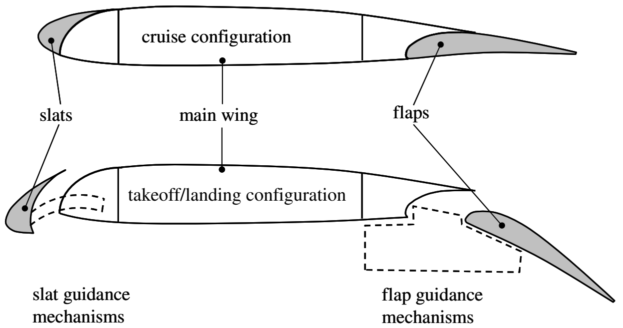

Fig. 2 Typical wing cross section with high-lift devices (slats and flaps).

kinematic and dynamic analysis of high-lift mechanisms, including analyses of interface loads and drive torques.

This paper is organized as follows:

1) Section II gives an overview about the equation of motion formulation used in MSC.Adams. The equations of motion are formulated for both rigid and flexible bodies. A modal approach is used to integrate linear-elastic bodies into the rigid-body system. Distributed airloads are applied to the linear-elastic bodies.

2) The technique of parametric model generation, allowing fast parameter adaptation for parameter studies, is described in Sec. III.

3) The model of the trailing edge, including the flaps with their guidance mechanisms, the flap support structure, the drive system, and the relevant airloads, is introduced in Sec. IV.

4) The leading-edge model, including the slats with their guidance mechanisms and airloads, is presented in Sec. V.

5) High-lift system simulation results are presented in Sec. VI.

6) A conclusion is given in Sec. VII.

II. Theoretical Background

This section briefly describes the theoretical background of multibody simulation. Within MSC.Adams, the equations of motion are formulated as differential algebraic equations. More detailed descriptions are found in [5–11]. Modern simulation programs allow the inclusion of flexible bodies in multibody models. Typically, a flexible body is described in the floating reference frame formulation, which is briefly explained. MSC.Adams uses the Craig–Bampton method to include FE models of flexible bodies into the multibody model formulation. Finally, the theory of the modal forces is described. This method allows force application directly to the FE model.

A. Dynamics of a Constrained System of Rigid Bodies

The position of the ith body of a constrained multibody system is described by a spatial vector $\hat{\mathbf{r}}_i$ consisting of the position vector $\mathbf{r}_i$ from an inertial system K_0 to a body-fixed coordinate system K_i, and $m_i \geq 3$, coordinates $\boldsymbol{\gamma}_i$, describing the spatial orientation of K_i relative to K_0:

$$\hat{\mathbf{r}}_i = \begin{bmatrix} \mathbf{r}_i \\ \boldsymbol{\gamma}_i \end{bmatrix} \tag{1}$$

Examples for the definition of $\boldsymbol{\gamma}_i$ are Euler angles or Euler parameters (unit quaternions). Accordingly, the absolute velocity of the ith body is described by the velocity $\mathbf{v}_i$ and the angular velocity $\boldsymbol{\omega}_i$ of K_i that are put together to the six-dimensional spatial vector:

$$\hat{\mathbf{v}}_i = \begin{bmatrix} \mathbf{v}_i \\ \boldsymbol{\omega}_i \end{bmatrix} \tag{2}$$

To describe the position and velocity of the overall system with N bodies, the vectors

$$\hat{\mathbf{r}} = \begin{bmatrix} \hat{\mathbf{r}}_1 \\ \vdots \\ \hat{\mathbf{r}}_N \end{bmatrix}, \qquad \hat{\mathbf{v}} = \begin{bmatrix} \hat{\mathbf{v}}_1 \\ \vdots \\ \hat{\mathbf{v}}_N \end{bmatrix} \tag{3}$$

are introduced. The relation between the time derivative of $\hat{\mathbf{r}}_i$ and $\hat{\mathbf{v}}_i$ is given by kinematic differential equations of the form

$$\dot{\hat{\mathbf{r}}}_i = \hat{\mathbf{H}}_i(\hat{\mathbf{r}}_i)\hat{\mathbf{v}}_i, \qquad i = 1, \ldots, N \quad \text{or} \quad \dot{\hat{\mathbf{r}}} = \hat{\mathbf{H}}(\hat{\mathbf{r}})\hat{\mathbf{v}}$$
$$\hat{\mathbf{H}} = \text{diag}(\hat{\mathbf{H}}_1, \ldots, \hat{\mathbf{H}}_N) \tag{4}$$

The constraints between the rigid bodies at the position, velocity, and acceleration levels are formulated in implicit form:

$$\mathbf{g}\,(\hat{\mathbf{r}}, t) = \mathbf{0} \tag{5}$$

$$\dot{\mathbf{g}} \equiv \mathbf{G}(\hat{\mathbf{r}}, t)\hat{\mathbf{v}} + \bar{\dot{\mathbf{g}}}(\hat{\mathbf{r}}, t) = \mathbf{0} \tag{6}$$

$$\ddot{\mathbf{g}} \equiv \mathbf{G}(\hat{\mathbf{r}}, t)\dot{\hat{\mathbf{v}}} + \bar{\ddot{\mathbf{g}}}(\hat{\mathbf{r}}, \hat{\mathbf{v}}, t) = \mathbf{0} \tag{7}$$

The kinetic differential equations are defined by the principles of momentum and moment of momentum. Using spatial force vectors $\hat{\mathbf{f}}_i$ containing a pair of a force and a torque, the kinetic equations of the ith body are

$$\hat{\mathbf{M}}_i \cdot \dot{\hat{\mathbf{v}}}_i = \hat{\mathbf{f}}_i^c + \hat{\mathbf{f}}_i^a + \hat{\mathbf{f}}_i^r, \qquad i = 1, \ldots, N \tag{8}$$

with the (6,6) mass matrix $\hat{\mathbf{M}}_i$, gyroscopic and Coriolis forces $\hat{\mathbf{f}}_i^c$, applied forces $\hat{\mathbf{f}}_i^a$, and reaction forces (constraint forces) $\hat{\mathbf{f}}_i^r$. The overall kinetic equations can be written as

$$\hat{\mathbf{M}} \cdot \dot{\hat{\mathbf{v}}} = \hat{\mathbf{f}}^c + \hat{\mathbf{f}}^e + \hat{\mathbf{f}}^r \quad \text{with} \quad \hat{\mathbf{M}} = \text{diag}(\hat{\mathbf{M}}_1, \ldots, \hat{\mathbf{M}}_n)$$
$$\hat{\mathbf{f}}^{c/a/r} = \begin{bmatrix} \hat{\mathbf{f}}_1^{c/a/r} \\ \vdots \\ \hat{\mathbf{f}}_N^{c/a/r} \end{bmatrix} \tag{9}$$

The reaction forces $\hat{\mathbf{f}}^r$ have components in the constrained spatial directions only, given by the row vectors of the constraint matrix $\mathbf{G}$ from Eq. (4). Accordingly, they can be expressed by means of the explicit reaction force equations

$$\mathbf{f}^{\,r} = \mathbf{G}^T\boldsymbol{\lambda} \tag{10}$$

with reaction force coordinates (Lagrange multipliers) $\boldsymbol{\lambda}$. If the positions $\hat{\mathbf{r}}$ and the velocities $\hat{\mathbf{v}}$, which have to be consistent with the constraints in Eq. (5) and their first-order time derivatives in Eq. (6), are given with Eqs. (7) and (8), together they represent a set of linear equations to uniquely determine the accelerations $\dot{\hat{\mathbf{v}}}$ and the reaction force coordinates $\boldsymbol{\lambda}$:

$$\begin{bmatrix} \hat{\mathbf{M}} & \mathbf{G}^T \\ \mathbf{G} & \mathbf{0} \end{bmatrix} \begin{bmatrix} \dot{\hat{\mathbf{v}}} \\ -\boldsymbol{\lambda} \end{bmatrix} = \begin{bmatrix} \hat{\mathbf{f}}^c + \hat{\mathbf{f}}^a \\ -\bar{\ddot{\mathbf{g}}} \end{bmatrix} \tag{11}$$

Numerical integration of the velocity $\hat{\mathbf{v}}$, obtained from the kinematic differential equation (4) and the acceleration $\dot{\hat{\mathbf{v}}}$ obtained from Eq. (11), yields the motion of the system described by the position $\hat{\mathbf{r}}(t)$ and the velocity $\hat{\mathbf{v}}(t)$. The reaction force coordinates $\boldsymbol{\lambda}$ obtained from Eq. (11) yield the reaction forces $\hat{\mathbf{f}}^r$ by means of the explicit reaction force Eq. (10). During numerical integration, the constraints at the position and velocity levels may be violated, and a constraint stabilization method has to be applied.

B. Dynamics of Linear-Elastic Bodies

If the elastic deflections of the bodies cannot be neglected, flexible bodies have to be included into the multibody model. The equations of motion of the rigid multibody system have to be extended appropriately. The way to obtain the equations of motion of a flexible body in the floating reference frame formulation is briefly described. The method is not restricted to a FE description of the flexible body. Generally, the motion of a point P on a flexible body can be described by a rigid-body motion and a motion caused by the flexibility of the body. As seen in Fig. 3, the position vector $\mathbf{r}_P$ of the point P on the ith body is composed of the position vector $\mathbf{r}_i$ of the body-fixed coordinate frame K_i, a vector $\mathbf{u}_0$ which describes the position of point P_0 on the undeformed body relative to K_i, and a vector $\mathbf{u}_P$ which describes the actual position P on the deformed body relative to P_0. Normally, vector $\mathbf{u}_P$ is described relative to the body-fixed coordinate frame K_i. In the case of a rigid body, the points P_0 and P coincide.

With the coordinate transformation matrix $\mathbf{T}_i(\boldsymbol{\gamma}_i)$ between the spatially-fixed coordinate frame K_0 and the body-fixed coordinate frame K_i, the position of point P is described by

$$\mathbf{r}_P = \mathbf{r}_i + \mathbf{T}_i\bar{\mathbf{u}} \quad \text{with} \quad \bar{\mathbf{u}} = \mathbf{u}_0 + \mathbf{u}_P \tag{12}$$

For the formulation of the equations of motion, the deformation vector $\mathbf{u}_P$ is typically expressed by a matrix of shape functions $\boldsymbol{\Phi}_i$ and a vector of elastic coordinates $\mathbf{q}_i$; both are related to the ith body

$$\mathbf{u}_P = \boldsymbol{\Phi}_i\mathbf{q}_i \tag{13}$$

and Eq. (12) becomes

$$\mathbf{r}_P = \mathbf{r}_i + \mathbf{T}_i\bar{\mathbf{u}} \quad \text{with} \quad \bar{\mathbf{u}} = \mathbf{u}_0 + \boldsymbol{\Phi}_i\mathbf{q}_i \tag{14}$$

Among the different methods to define the shape function matrix $\boldsymbol{\Phi}_i$, modal superposition is considered. Here, the matrix $\boldsymbol{\Phi}_i$ is identical to the modal matrix of the body, and the flexible coordinates $\mathbf{q}_i$ are the modal coordinates. However, the results obtained with this method are insufficient in the case of static loads. Therefore, a combination of static and dynamic modes is implemented in commercial simulation tools. MSC.Adams uses the so-called Craig–Bampton method, which is briefly described in Sec. II.C. There exist other methods to describe the deformation kinematics (see [12,13]).

According to Shabana [8], the mass and stiffness matrices of the overall system can be built up by using the kinetic and potential energies of the flexible bodies. To formulate the kinetic energy, the velocity $\dot{\mathbf{r}}_P$ of P is needed, which is obtained by differentiation of Eq.(14) with respect to the time

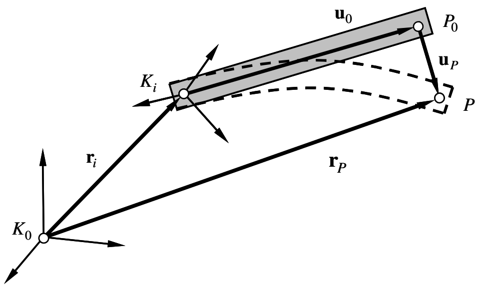

Fig. 3 Kinematics of a flexible body [8].

$$\dot{\mathbf{r}}_P = \mathbf{v}_P = \dot{\mathbf{r}}_i + \dot{\mathbf{T}}_i\bar{\mathbf{u}} + \mathbf{T}_i\boldsymbol{\Phi}_i\dot{\mathbf{q}}_i \quad \text{with} \quad \bar{\mathbf{u}} = \mathbf{u}_0 + \boldsymbol{\Phi}_i\mathbf{q}_i \tag{15}$$

The time derivatives of the rigid-body position vector $\mathbf{u}_0$ and the shape function matrix $\boldsymbol{\Phi}_i$ vanish, as their representations in the body-fixed coordinate frame K_i are constant. The time derivative of the transformation matrix $\dot{\mathbf{T}}_i$ can be expressed in terms of the time derivatives of the rotation coordinates $\dot{\boldsymbol{\gamma}}_i$ of K_i. The middle summand on the right-hand side of Eq. (5) can then be expressed in the form

$$\dot{\mathbf{T}}_i\bar{\mathbf{u}} = \mathbf{B}_i\dot{\boldsymbol{\gamma}}_i \tag{16}$$

with the matrix $\mathbf{B}_i$ obtained from

$$\mathbf{B}_i = \left[\frac{\partial}{\partial\gamma_{i,1}}(\mathbf{T}_i\bar{\mathbf{u}}),\ \ldots,\ \frac{\partial}{\partial\gamma_{i,m_i}}(\mathbf{T}_i\bar{\mathbf{u}})\right] \tag{17}$$

With Eq. (16), the velocity $\dot{\mathbf{r}}_P$ in Eq. (15) can be written as

$$\dot{\mathbf{r}}_P = \dot{\mathbf{r}}_i + \mathbf{B}_i\dot{\boldsymbol{\gamma}}_i + \mathbf{T}_i\boldsymbol{\Phi}_i\dot{\mathbf{q}}_i \tag{18}$$

or in matrix form

$$\dot{\mathbf{r}}_P = [\,\mathbf{I} \quad \mathbf{B}_i \quad \mathbf{T}_i \quad \boldsymbol{\Phi}_i\,] \begin{bmatrix} \dot{\mathbf{r}}_i \\ \dot{\boldsymbol{\gamma}}_i \\ \dot{\mathbf{q}}_i \end{bmatrix} = \mathbf{L}_i\dot{\tilde{\mathbf{q}}}_i \tag{19}$$

with the identity matrix $\mathbf{I}$ and the overall coordinate vector $\dot{\tilde{\mathbf{q}}}_i$ of the ith body.

The kinetic energy T_i of the ith body is defined as

$$T_i = \frac{1}{2}\int_{V_i} \rho\dot{\mathbf{r}}_P^T\dot{\mathbf{r}}_P\,\mathrm{d}V \tag{20}$$

with the volume V_i and the density ρ. With Eq. (19), the kinetic energy becomes

$$T_i = \frac{1}{2}\int_{V_i} \rho\dot{\tilde{\mathbf{q}}}_i^T\mathbf{L}_i^T\mathbf{L}_i\dot{\tilde{\mathbf{q}}}_i\,\mathrm{d}V = \frac{1}{2}\dot{\tilde{\mathbf{q}}}_i^T\left[\int_{V_i} \rho\mathbf{L}_i^T\mathbf{L}_i\,\mathrm{d}V\right]\dot{\tilde{\mathbf{q}}}_i \tag{21}$$

The expression between the squared brackets on the right-hand side of Eq. (21) is the mass matrix $\mathbf{M}_i$ of the flexible body. With matrix $\mathbf{L}_i$ from Eq. (19), it reads:

$$\mathbf{M}_i = \int_{V_i} \rho \begin{bmatrix} \mathbf{I} & \mathbf{B}_i & \mathbf{T}_i\boldsymbol{\Phi}_i \\ & \mathbf{B}_i^T\mathbf{B}_i & \mathbf{B}_i^T\mathbf{T}_i\boldsymbol{\Phi}_i \\ \text{symmetric} & & \boldsymbol{\Phi}_i^T\boldsymbol{\Phi}_i \end{bmatrix} \mathrm{d}V \tag{22}$$

or with abbreviated submatrices

$$\mathbf{M}_i = \int_{V_i} \rho \begin{bmatrix} \mathbf{m}_{rr} & \mathbf{m}_{r\gamma} & \mathbf{m}_{rq} \\ & \mathbf{m}_{\gamma\gamma} & \mathbf{m}_{\gamma q} \\ \text{symmetric} & & \mathbf{m}_{qq} \end{bmatrix} \mathrm{d}V \tag{23}$$

Note that the offdiagonal submatrices of $\mathbf{M}_i$ are nonzero. They describe inertia couplings between the rigid-body motion of the multibody system and the motion of the flexible body. The submatrices $\mathbf{m}_{rr}$ associated with the translational velocity $\dot{\mathbf{r}}_i$ of the body-fixed coordinate frame K_i and $\mathbf{m}_{qq}$ associated with the flexible coordinates $\mathbf{q}_i$ are constant.

The potential energy of a flexible body consists of its potential energy in the gravity field and the deformation energy. The latter is used to calculate the stiffness matrix. For that purpose, the internal virtual work of the ith flexible body is formulated

$$\delta W_i = -\int_{V_i} \boldsymbol{\sigma}^T\delta\boldsymbol{\varepsilon}\,\mathrm{d}V \tag{24}$$

where $\boldsymbol{\sigma}$ is the stress vector and $\delta\boldsymbol{\varepsilon}$ represents the virtual strain. The strain $\boldsymbol{\varepsilon}$ can be expressed in terms of the displacement $\mathbf{u}_P$ from Eq. (13) by means of the deformation tensor $\mathbf{D}$:

$$\boldsymbol{\varepsilon} = \mathbf{D}\mathbf{u}_P \tag{25}$$

whereby $\mathbf{u}_P$ is given in terms of the shape functions $\boldsymbol{\Phi}_i$ by means of Eq. (13). For linear isotropic material, the constitutive equations as Hooke's law, under consideration of Eq. (25), can be written as

$$\boldsymbol{\sigma} = \mathbf{E}\boldsymbol{\varepsilon} \quad \text{or} \quad \boldsymbol{\sigma} = \mathbf{E}\mathbf{D}\boldsymbol{\Phi}_i\mathbf{q}_i \tag{26}$$

Inserting Eq. (25) and (26) into Eq. (24) yields the virtual work

$$\begin{aligned}\delta W_i &= -\int_{V_i} \mathbf{q}_i^T(\mathbf{D}_i\boldsymbol{\Phi}_i)^T\mathbf{E}\mathbf{D}_i\boldsymbol{\Phi}_i\delta\mathbf{q}_i\,\mathrm{d}V \\ &= -\mathbf{q}_i^T\left[\int_{V_i}(\mathbf{D}_i\boldsymbol{\Phi}_i)^T\mathbf{E}\mathbf{D}_i\boldsymbol{\Phi}_i\,\mathrm{d}V\right]\delta\mathbf{q}_i\end{aligned} \tag{27}$$

The expression between the squared brackets on the right-hand side of Eq. (27) represents the stiffness matrix $\mathbf{k}_{qq}$ belonging to the flexible coordinates $\mathbf{q}_i$ of the ith body. It is a submatrix of the overall stiffness matrix of the flexible body that is defined in analogy to Eq. (21) by using Eqs. (24–27) under consideration of the complete set of coordinates $\tilde{\mathbf{q}}_i$ of the ith flexible body:

$$\delta W_i = -\overbrace{[\mathbf{r}_i^T \quad \boldsymbol{\gamma}_i^T \quad \mathbf{q}_i^T]}^{\tilde{\mathbf{q}}_i^T}\overbrace{\begin{bmatrix}\mathbf{0} & \mathbf{0} & \mathbf{0}\\ \mathbf{0} & \mathbf{0} & \mathbf{0}\\ \mathbf{0} & \mathbf{0} & \mathbf{k}_{qq}\end{bmatrix}}^{\tilde{\mathbf{K}}_i}\begin{bmatrix}\delta\mathbf{r}_i\\ \delta\boldsymbol{\gamma}_i\\ \delta\mathbf{q}_i\end{bmatrix} \tag{28}$$

The square matrix on the right-hand side represents the stiffness matrix $\mathbf{K}_\mathrm{i}$ of the ith flexible body. From Eq. (28), it follows that there is no stiffness coupling between the flexible coordinates $\mathbf{q}_i$ and the rigid-body coordinates $\mathbf{r}_i$ and $\boldsymbol{\gamma}_i$ of the flexible body. The overall potential energy of the ith flexible body is obtained as

$$U_i = \int_{V_i}\rho\mathbf{r}_P^T\mathbf{g}\,\mathrm{d}V + \frac{1}{2}\mathbf{q}_i^T\tilde{\mathbf{K}}_i\mathbf{q}_i \tag{29}$$

in which the first summand represents the potential energy of the body in a gravity field (gravity vector $\mathbf{g}$). The equations of motion of the overall multibody system are formulated in terms of the rigid body and elastic coordinates of all N bodies

$$\tilde{\mathbf{q}} = \begin{bmatrix}\mathbf{r}\\ \boldsymbol{\gamma}\\ \mathbf{q}\end{bmatrix} \quad \text{with} \quad \mathbf{r} = \begin{bmatrix}\mathbf{r}_1\\ \vdots\\ \mathbf{r}_N\end{bmatrix}, \quad \boldsymbol{\gamma} = \begin{bmatrix}\boldsymbol{\gamma}_1\\ \vdots\\ \boldsymbol{\gamma}_N\end{bmatrix}, \quad \mathbf{q} = \begin{bmatrix}\mathbf{q}_1\\ \vdots\\ \mathbf{q}_N\end{bmatrix} \tag{30}$$

With the Lagrange function

$$L = T - U \quad \text{with} \quad T = \sum_{i=1}^{N} T_i, \qquad U = \sum_{i=1}^{N} U_i \tag{31}$$

the equations of motion are obtained in terms of $\tilde{\mathbf{q}}$ by means of Lagrange's equations of the second kind

$$\frac{\mathrm{d}}{\mathrm{d}t}\left(\frac{\partial L}{\partial\dot{\tilde{\mathbf{q}}}}\right)^T - \left(\frac{\partial L}{\partial\tilde{\mathbf{q}}}\right)^T = \mathbf{Q}^a + \mathbf{Q}^r \tag{32}$$

with the generalized nonconservative applied forces $\mathbf{Q}^a$, and the generalized reaction forces $\mathbf{Q}^r$. The evaluation of Eq. (32) leads to the typical structure of the equations of motion

$$\begin{aligned}&\begin{bmatrix}\mathbf{M}_{rr} & \mathbf{M}_{r\gamma} & \mathbf{M}_{rq}\\ \mathbf{M}_{\gamma r} & \mathbf{M}_{\gamma\gamma} & \mathbf{M}_{\gamma q}\\ \mathbf{M}_{qr} & \mathbf{M}_{q\gamma} & \mathbf{M}_{qq}\end{bmatrix}\begin{bmatrix}\ddot{\mathbf{r}}\\ \ddot{\boldsymbol{\gamma}}\\ \ddot{\mathbf{q}}\end{bmatrix} + \begin{bmatrix}\mathbf{0} & \mathbf{0} & \mathbf{0}\\ \mathbf{0} & \mathbf{0} & \mathbf{0}\\ \mathbf{0} & \mathbf{0} & \mathrm{k}_{\mathbf{qq}}\end{bmatrix}\begin{bmatrix}\mathbf{r}\\ \boldsymbol{\gamma}\\ \mathbf{q}\end{bmatrix}\\ &\quad = \mathbf{Q}^c + \mathbf{Q}^a + \mathbf{Q}^r\end{aligned} \tag{33}$$

with the generalized Coriolis forces $\mathbf{Q}_i^c$. In analogy to Eq. (10), the generalized reaction forces $\mathbf{Q}^r$ are expressed in terms of reaction force coordinates (Lagrange multipliers) $\boldsymbol{\lambda}$ by explicit constraint force equations of the form [8]

$$\mathbf{Q}^r = \mathbf{G}_{\tilde{q}}^T\boldsymbol{\lambda} \tag{34}$$

The constraint matrix $\mathbf{G}_{\tilde{\mathbf{q}}}$ is obtained from the time derivatives of the implicit constraint equations in terms of the overall coordinates $\tilde{\mathbf{q}}$ in analogy to Eq. (6).

C. Craig–Bampton Method

To formulate the equations of motion of a flexible multibody system, according to the previous section, an appropriate description of a flexible body is needed. MSC.Adams is able to import flexible-body models generated as FE systems after conversion by means of the Craig–Bampton method (see also [14]). In contrast to a continuum, a FE body consists of a discrete number of points (nodes). This means the n discrete points of the ith body can be summarized to

$$\mathbf{u}_i = [\mathbf{u}_{P1} \quad \cdots \quad \mathbf{u}_{Pn}]^T \tag{35}$$

Normally, a FE body consists of more DOF than a complete multibody system. The purpose of the Craig–Bampton method is to find shape functions $\boldsymbol{\Phi}_i$ in such a manner that both Eq. (13) is adequately satisfied and the DOF are significantly reduced. The Craig–Bampton method combines modal superposition and static shapes. The displacements $\mathbf{u}_i$ of the ith body are partitioned into displacements of the boundary DOF $\mathbf{u}_{Bi}$ and interior DOF $\mathbf{u}_{Ii}$, thus $\mathbf{u}_i = [\mathbf{u}_{Bi} \quad \mathbf{u}_{Ii}]^T$. The boundary DOF, selected by the user, are normally the interconnection points of the flexible body with other components of the multibody model. There are two sets of mode shapes defined in the Craig–Bampton method: the constraint modes and the fixed boundary normal modes.

The constraint modes are static shapes. They are calculated by giving each boundary DOF a unit displacement while fixing all other boundary DOF. The basis of the constraint modes consists of all possible motions of the boundary DOF. The modal coordinates of the constraint modes $\mathbf{q}_{Ci}$ correspond to the displacements of the boundary DOF $\mathbf{q}_{Ci} = \mathbf{u}_{Bi}$.

The fixed boundary normal modes are mode shapes with corresponding modal coordinates $\mathbf{q}_{Ni}$. To obtain these mode shapes, the boundary DOF are fixed, and the eigenvalue problem is solved. The number of mode shapes and corresponding eigenfrequencies equals the DOF number of a flexible body. Depending on the particular modeling objectives, the user defines the number of mode shapes. The quality of the results will be improved by increasing the number of fixed boundary normal modes taken into account.

For the ith body, the relationship between the physical DOF $\mathbf{u}_i$ and the modal coordinates $\mathbf{q}_i = [\mathbf{q}_{Ci} \quad \mathbf{q}_{Ni}]^T$ of the Craig–Bampton modes are represented by

$$\begin{bmatrix}\mathbf{u}_{Bi}\\ \mathbf{u}_{Ii}\end{bmatrix} = \begin{bmatrix}\mathbf{I} & \mathbf{0}\\ \boldsymbol{\Phi}_{ICi} & \boldsymbol{\Phi}_{INi}\end{bmatrix}\begin{bmatrix}\mathbf{q}_{Ci}\\ \mathbf{q}_{Ni}\end{bmatrix} \quad \text{or} \quad \mathbf{u}_i = \hat{\boldsymbol{\Phi}}_i\mathbf{q}_i \tag{36}$$

The components of $\boldsymbol{\Phi}_{ICi}$ are the physical displacements of the interior DOF in the constraint modes, and the components of $\boldsymbol{\Phi}_{IN}$ are the physical displacements of the interior DOF in the fixed boundary normal modes. The subscripts I, B, N, and C denote the internal DOF, boundary DOF, fixed boundary normal modes, and constraint modes, respectively.

To get the generalized stiffness and mass matrices corresponding to the Craig–Bampton modal basis, a modal transformation by means of Eq. (36) is necessary. The generalized stiffness matrix is then obtained as

$$\begin{aligned}\hat{\mathbf{K}}_i = \hat{\boldsymbol{\Phi}}_i^T\mathbf{K}_i\hat{\boldsymbol{\Phi}}_i &= \begin{bmatrix}\mathbf{I} & \mathbf{0}\\ \boldsymbol{\Phi}_{ICi} & \boldsymbol{\Phi}_{INi}\end{bmatrix}^T\begin{bmatrix}\mathbf{K}_{BBi} & \mathbf{K}_{BIi}\\ \mathbf{K}_{IBi} & \mathbf{K}_{IIi}\end{bmatrix}\begin{bmatrix}\mathbf{I} & \mathbf{0}\\ \boldsymbol{\Phi}_{ICi} & \boldsymbol{\Phi}_{INi}\end{bmatrix}\\ &= \begin{bmatrix}\hat{\mathbf{K}}_{CCi} & \mathbf{0}\\ \mathbf{0} & \hat{\mathbf{K}}_{NNi}\end{bmatrix}\end{aligned} \tag{37}$$

whereas the generalized mass matrix is calculated by

$$\hat{\mathbf{M}}_i = \hat{\boldsymbol{\Phi}}_i^T \mathbf{M}_i \hat{\boldsymbol{\Phi}}_i = \begin{bmatrix} \mathbf{I} & \mathbf{0} \\ \boldsymbol{\Phi}_{ICi} & \boldsymbol{\Phi}_{INi} \end{bmatrix}^T \begin{bmatrix} \mathbf{M}_{BBi} & \mathbf{M}_{BIi} \\ \mathbf{M}_{IBi} & \mathbf{M}_{IIi} \end{bmatrix} \begin{bmatrix} \mathbf{I} & \mathbf{0} \\ \boldsymbol{\Phi}_{ICi} & \boldsymbol{\Phi}_{INi} \end{bmatrix} = \begin{bmatrix} \hat{\mathbf{M}}_{CCi} & \hat{\mathbf{M}}_{NCi} \\ \hat{\mathbf{M}}_{CNi} & \hat{\mathbf{M}}_{NNi} \end{bmatrix} \tag{38}$$

The Craig–Bampton constraint modes are calculated by a static FE analysis. As a consequence, no eigenfrequencies are allocated to these modes. To assign corresponding frequencies to those static shapes, a subsequent mode shape orthonormalization is done. Therefore, a new eigenvalue problem in the modal space has to be solved with the modal coordinates $\mathbf{q}_i = [\mathbf{q}_{Ci} \quad \mathbf{q}_{Ni}]^T$ and the generalized mass and stiffness matrices $\hat{\mathbf{M}}_i$ and $\hat{\mathbf{K}}_i$:

$$\hat{\mathbf{K}}_i \bar{\mathbf{q}}_i = \lambda \hat{\mathbf{M}}_i \bar{\mathbf{q}}_i \tag{39}$$

The resulting eigenvectors $\bar{\mathbf{q}}_i$ can be arranged in a modal matrix $\mathbf{N}_i$. There is a natural frequency corresponding to every resulting eigenvector. The modal coordinates $\mathbf{q}_i$ can also be calculated as a superposition of all calculated eigenvectors with Craig–Bampton modal coordinates $\mathbf{q}_i^*$:

$$\mathbf{q}_i = \mathbf{N}_i \mathbf{q}_i^* \tag{40}$$

As a result, the physical displacements of the elastic body $\mathbf{u}_i$ from Eq. (36) can be expressed by

$$\mathbf{u}_i = \boldsymbol{\Phi}_i^* \mathbf{q}_i^* \quad \text{with} \quad \boldsymbol{\Phi}_i^* = \hat{\boldsymbol{\Phi}}_i \mathbf{N}_i \tag{41}$$

in which the columns of the matrix $\boldsymbol{\Phi}_i^*$ are the orthogonalized Craig–Bampton modes. In the elastic multibody formulation of Sec. II.B, Eq. (41) replaces Eq. (13) with the shape function matrix $\boldsymbol{\Phi}_i^*$ for the discrete points of the flexible body and the Craig–Bampton modal coordinates $\mathbf{q}_i^*$ as the elastic coordinates. The Craig–Bampton approach can be compared with modal superposition, which describes the motion of flexible body by its mode shapes [15]. However, the Craig–Bampton modes $\boldsymbol{\Phi}_i^*$ are not eigenvectors of the original physical system, and the corresponding Craig–Bampton natural frequencies are not the natural frequencies of the physical model of the flexible body.

D. Applying Distributed Loads to Linear-Elastic Bodies

To apply loads on elastic bodies, there are two methods available in MSC.Adams. The first method is to apply single forces or moments on each node of the elastic body in the multibody environment. The second method is to apply distributed forces in the FE environment and transfer them to the multibody program in which they are encapsulated in a force element called MFORCE. The second method is more efficient as MSC.Adams handles only one object and, as it is possible to create different load sets for the same FE model, allows switching between different load sets more easily. Therefore, it is used in the following. Disadvantages of the second method are that the forces cannot be visualized, the physical values of the applied forces cannot be measured in MSC.Adams, and the forces depend on the number of Craig–Bampton modes.

As the forces are applied on the FE model, the description starts with the equation of motion of the FE model of the *i*th flexible body (see also [16,17]):

$$\mathbf{M}_i \ddot{\mathbf{u}}_i + \mathbf{K}_i \mathbf{u}_i = \mathbf{F}_i \tag{42}$$

The matrices $\mathbf{M}_i$ and $\mathbf{K}_i$ are the mass and the stiffness matrices of the body in the FE software. The vector $\mathbf{u}_i$ represents the physical nodal displacements of the body, and the vector $\mathbf{F}_i$ contains the nodal loads. Structural damping is neglected because it is assumed to be small.

The equation of motion (42) can be transferred into modal space using Eq. (13) or into Craig–Bampton representation using Eq. (41). The shape function matrix $\boldsymbol{\Phi}_i$ is obtained as the solution of the eigenvalue problem of the free equation of motion (42) of the FE model, or as the shape function matrix $\boldsymbol{\Phi}_i^*$ of the orthogonalized Craig–Bampton modes from Eq. (41), respectively. The following formulations are written with the matrix $\boldsymbol{\Phi}_i$, but they also hold with the matrix $\boldsymbol{\Phi}_i^*$. As the shape function matrix $\boldsymbol{\Phi}_i$ is time independent, the time derivatives of the node displacements $\mathbf{u}_i$ are immediately obtained from the time derivatives of the modal coordinates $\mathbf{q}_i$. Insertion of Eq. (13) into Eq. (42) and premultiplication with $\boldsymbol{\Phi}_i^T$ lead to

$$\boldsymbol{\Phi}_i^T \mathbf{M}_i \boldsymbol{\Phi}_i \ddot{\mathbf{q}}_i + \boldsymbol{\Phi}_i^T \mathbf{K}_i \boldsymbol{\Phi}_i \mathbf{q}_i = \boldsymbol{\Phi}_i^T \mathbf{F}_i \tag{43}$$

or, if written with new matrices,

$$\hat{\mathbf{M}}_i \ddot{\mathbf{q}}_i + \hat{\mathbf{K}}_i \mathbf{q}_i = \mathbf{f}_i \tag{44}$$

The matrices $\hat{\mathbf{M}}_i$ and $\hat{\mathbf{K}}_i$ are called modal mass and stiffness matrices, respectively, and the vector $\mathbf{f}_i$ represents the modal load vector containing the modal forces. For further information about modal transformations, see [15,18,19].

III. Parametric Model Building of the High-Lift System

It is possible to import a multibody model into the simulation program MSC.Adams as an ASCII file, called a command file. This ASCII file is created by a MATLAB® script. The MATLAB script is structured into parameter and topology files. The parameter files contain all physical parameters of the multibody model, like transmission shaft diameters, design point coordinates, masses, and inertias. The topology files describe the assembly of the model by creating bodies and their connections to other bodies. There also exists a group of general element files. They contain functions to create multibody elements like joints, gears, or special types of bodies (links and plates).

The flexible bodies are created as FE models by means of the FE program MD Nastran. It is also possible to import ASCII files into MD Nastran, called bulk data files. The principle of model generation of the flexible bodies is equivalent to the generation of the command files for MSC.Adams. Consequently, the flexible bodies will be created by the same script that creates the command file. MD Nastran is automatically called by the MATLAB script. A result file called modal neutral file is obtained, which can be imported by MSC.Adams. This method ensures consistency. By using the same parameter files for generation of the input files for the multibody and FE models, the interface points between rigid and elastic components have identical coordinates. It is also possible to use the same reference frames for the multibody and FE models. The disadvantage of this method is that ill-conditioned FE models may be built up. Because it is difficult to check the condition of a flexible body in MSC.Adams, it is recommendable to check the flexible bodies with MSC.Patran before they are imported into MSC.Adams.

The stiffness of the flexible bodies is not finally specified at the current development level of the aircraft. For example, the side struts of the flap and slat bodies that support loads in spanwise direction are not yet defined in the current design status. Consequently, the stiffness of the flexible bodies is partly extracted from FE models of the high-lift system of previous aircraft models.

The airload data are generated by means of computational fluid dynamics (CFD) simulations. These data are imported by the MATLAB script and integrated into the parameter files. The schematic representation of the parametric model building is shown in Fig. 4.

The overall elastic multibody model consists of the command file and the modal neutral files of the flexible bodies. There are entries in the command file that call the modal neutral files of the flexible bodies. Consequently, the modal neutral files and the flexible bodies, respectively, are automatically integrated into the model when the command file is imported into MSC.Adams.

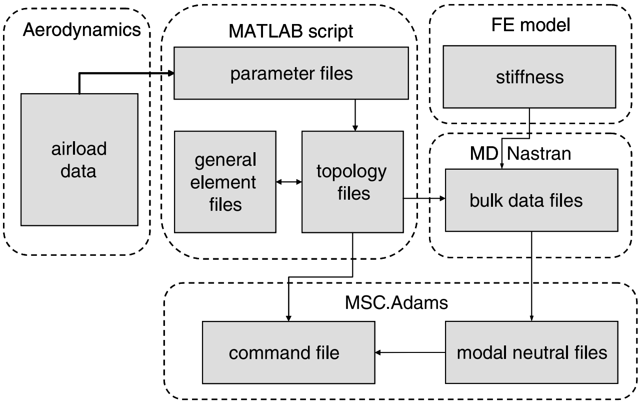

Fig. 4 Methodology of model generation.

The described parametric model building has the great advantage to facilitate parameter studies. The disadvantage is the effort to create the parametric model. If no parameter changes are planned, it would be easier to create a model directly by using the graphic user interface of MSC.Adams.

IV. Multibody Model of the Wing Trailing Edge

The high-lift devices of the aircraft comprise the two flaps, the support structure, and the drive mechanisms at the trailing edge of the wing (Fig. 1). Because of symmetry, the left wing is modeled only. The flaps are supported by tracks with mechanisms that move them into the desired positions. The inboard flap is supported by tracks 1 and 2, and the outboard flap by tracks 3, 4, and 5. In this section, the multibody models of the guidance mechanisms of the flaps, the corresponding transmission systems, and the application of airloads are described.

A. Flap Guidance Mechanisms

The extension motion of the flaps comprises a translational and a rotational motion. According to Rudolph [3], the translational part of the extension motion of the flap is called Fowler motion. The translational motion is needed for takeoff to increase the wing area. The rotation at the end of the Fowler motion is needed in the landing configuration to increase the curvature of the wing. This leads to an increased aerodynamic drag in order to slow down the aircraft.

As seen from the schematic representation of the kinematics of the inboard flap in Fig. 5 and of the outboard flap in Fig. 6, the Fowler motion is realized by two different mechanism designs for track 1 of the inboard flap and for the four other tracks. The different designs are mainly caused by the more confined design space for track 1, which is located within the wing nacelle, whereas the other four tracks are fixed under the wing.

The mechanism of track 1 supports the flap structure with two ball points moving along two curved paths called upper and lower traces (Fig. 5). The flap first moves translational while it rotates at the end of the curves, because the distance of the traces increases.

The mechanisms of tracks 2 to 5 are essentially four-bar linkages. Two variants are distinguished in order to avoid an overconstrained system leading to excessive joint forces in the case of elastic deformations of the mechanism components and of the wing structure (Fig. 7). Both mechanism variants support the flap structure on a translationally moving carriage driven by the rotating lever arm via a drive strut and a pendulum support at the rear end. The two mechanism variants differ in the connection between the flap structure and

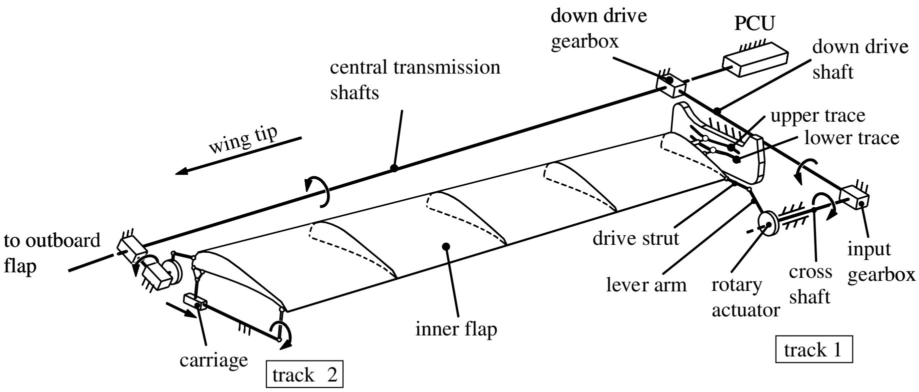

Fig. 5 Kinematics of the inboard flap.

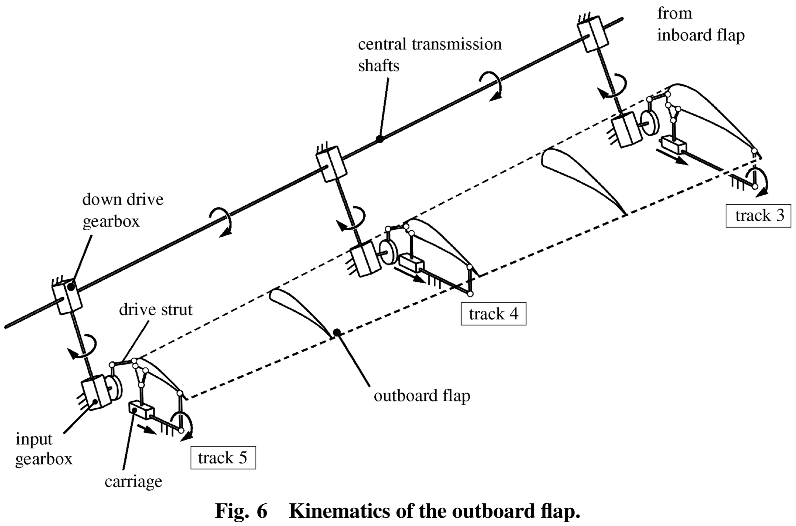

Fig. 6 Kinematics of the outboard flap.

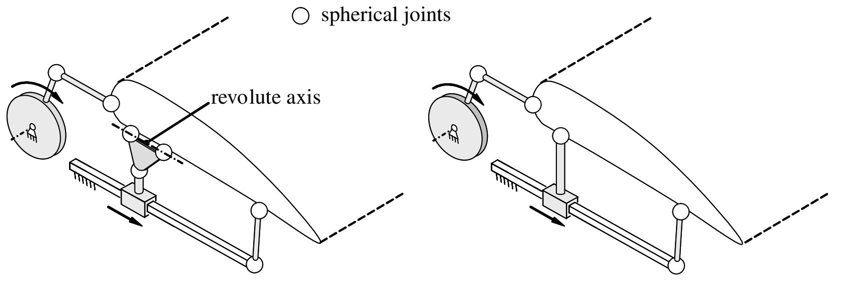

a) Tracks 2, 3, 5:
movable in spanwise direction

b) Track 4:
fixed in spanwise direction

Fig. 7 Mechanisms of tracks 2 to 5.

the carriage. The mechanisms of tracks 2, 3, and 5 are modeled by an intermediate linkage, that can be regarded as a combination of a spherical and a revolute joint, allowing a motion in spanwise direction. The mechanism of track 4 uses a single spherical joint instead that provides a fixed support of the outboard flap in spanwise direction. The support of the inboard flap in spanwise direction is provided by track 1.

B. Multibody Modeling of the Flap Mechanisms

The multibody model of the flap system is built up, as seen in Figs. 5 and 6. To avoid identical DOF occurring for struts with spherical joints at both ends, universal joints with two DOF are appropriately introduced. The plate with the curved paths of track 1 (Fig. 5) is modeled as a rigid body with fixed splines for the upper and lower traces. The rigid-body model is used as there is no possibility in MSC.Adams to fix a spline on an elastic body. The flap structure is connected with the splines by means of point-to-curve constraints. A point-to-curve constraint represents a spherical joint moving along a given path.

As tracks 2 to 5 undergo larger elastic deformations, they are modeled as flexible bodies with the method of FEs. A simple beam model is created with MD Nastran for that purpose. A beam model represents the mechanical properties of a body by reducing the volume to a line. This line is normally modeled in the area center of the cross section and contains elastic properties like bending stiffness or extensional stiffness.

Because the beam model does not have any volume expansion, it cannot be directly integrated into the multibody model. Therefore, interface elements using MD Nastran have to be modeled to create connections between the elastic beam models and the rigid bodies. The interface elements are built up as beam elements that are almost rigid and have a negligible mass to minimize the influence on the modal analysis.

The flaps are modeled as beam models with MD Nastran. A schematic representation of a cross section of a flap body is given in Fig. 8. The beam is not located in the area center but in the shear center. One of the main objectives of this model is to include the torsion of the flap bodies. The rotation axis of a thin-walled shell structure with closed cross section is located near this axis. This approach is chosen as detailed properties of the flap bodies are not yet available.

Rigid elements connect the beam with the nose point, the trailing edge, and the area center of the flap. Concentrated mass elements are attached in the center area, which is identical to the center of gravity, in case of homogeneous density. The rigid elements from the shear center to the nose points are needed for a unified load application point. The elements to the trailing edge are needed to measure the deformation of the flap bodies at this line, which has to be limited because of aerodynamic requirements.

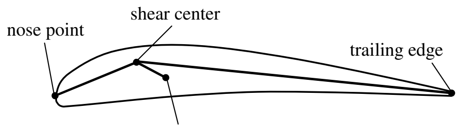

Fig. 8 Cross section of a flap.

The objective of the beam model is to represent the dynamic and static behavior of the real flap. It is obvious that the beam model describes the global deformation of a flap body only while it is not able to reproduce higher natural modes and higher natural DOF. To take these deformations into account, a shell or volume model has to be created.

In case of a failure of the trailing-edge mechanisms, an alternative load path via an interconnection strut between the inboard and outboard flaps becomes active (Fig. 9). The interconnection strut consists of an indenter that moves in a tubular casing with a defined free travel in both directions and energy-dissipating end stops. During nominal operation of the flap system, the motion of the indenter is within the free travel, and the interconnection strut is not active. If a drive strut of the flap tracks fails, one of the free travel limits is exceeded, and the free motion of the flap is cushioned by the end stop.

The multibody model of the interconnection strut consists of two cylindrical bodies connected with a prismatic joint. The end stops of the interconnection strut are modeled by a two-sided force element with a dead zone, called the BISTOP element in MSC.Adams. In the failure case, the limits of the dead zone are exceeded, and a dissipative contact force, depending on the relative position and velocity, occurs.

C. Transmission System of the Trailing Edge

At the current development level, the drive system, also called the transmission system, consists of one central shaft system and five downdrive stations, as seen in Figs. 1, 5, and 6. The shaft system is driven by an electrohydraulic actuator unit, called the power control unit (PCU), that is installed in the middle between the wings and at the bottom of the nacelle. For reasons of redundancy, the PCU consists of two independent electrohydraulic drives.

To compare design variants of the transmission system, three versions are integrated into the multibody model. The first model holds for the central shaft system represented in Figs. 5 and 6. The shafts are modeled as cylindrical sections that are connected by universal and prismatic joints, respectively. The shaft system is mounted with spherical joints on the wing structure. As long as the wing is not yet modeled as an elastic body, the mount points of the shaft system are spatially fixed. The second transmission model

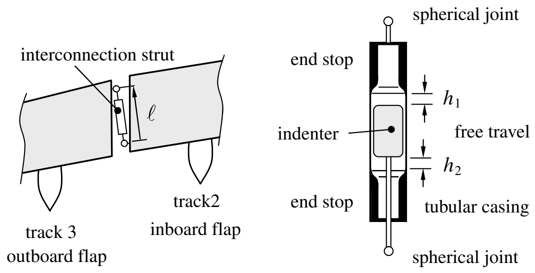

Fig. 9 Interconnection strut.

comprises individual actuators for each flap. Therefore, the shaft sections between tracks 2 and 3 are removed, and individual PCUs are connected to the shaft systems of the inboard and outboard flaps. The third transmission model consists of the downdrive stations only, and all central transmission shafts are removed. This version is used to reduce the simulation time when the transmission system is not to be considered.

A downdrive station comprises the downdrive gearbox, the input gearbox, the cross shaft, and the rotary gear actuator (Figs. 5 and 6). The downdrive gearbox is a T-gearbox that transfers the central shaft rotation to the actuators. In MSC.Adams, the rotation of the central shaft system is transferred to the downdrive shaft via a coupler element that connects the relative coordinates of two joints. A coupler also allows a gear ratio between the two joint coordinates. The downdrive shaft connects the downdrive gearbox with the input gearbox. The input gearbox is angular and mounted on the corresponding track structure with two bushing elements. In MSC.Adams, a bushing is a six-dimensional spring-damper element composed of three translational and three rotational spring-damper elements. The input gearbox is connected with the rotary gear actuator via the cross shaft. In the model, the rotation of the downdrive shaft is transmitted to the cross shaft with a coupler. The rotary actuator is a planetary gear, modeled as a coupler, that transfers the rotation of the cross shaft to the rotational degree of the lever arm, which drives the corresponding track mechanism (Figs. 5 and 6).

The transmission systems as described previously are modeled by rigid bodies. To integrate a torsional stiffness, the shafts are separated into two sections that are connected by a revolute joint and a torsional spring. For the third transmission model with individual actuations for each track, the resulting torsional stiffness of the central transmission shaft sections are connected as a series and implemented into the downdrive shaft sections. Altogether, six different transmission systems are available in the model of the flap system, comprising the three rigid transmission systems previously described and the corresponding three transmission systems with torsional stiffness.

D. Airloads on the Flaps

The airloads are provided separately by a CFD simulation and wind-tunnel tests. The simulated pressure distribution is converted to a resulting load force and torque vector. These loads are the basis for the airloads that are applied on the elastic multibody system. An interaction between the loads and the deformation of the wing is neglected. Thus, the pressure distribution results from a CFD simulation with a rigid wing in the reference configuration.

Because of the simple beam model used for the flap model, it is not possible to apply the resulting airloads in the load attack point of the real flap. Instead, all loads are transferred to a standardized load attack point, which is the nose point of the beam model (Fig. 10).

The resulting load force is split up into two components acting in chordwise and normal directions. The chord is defined by a line between the nose point and the trailing-edge point. To make this force equivalent to the load in the real load attack point, a correction moment is applied to the flap body. The correction moment is calculated by the value of the normal force, and the distance between the real load attack point and the nose point. The loads are applied to the FE model of the flap bodies and transferred to modal forces, as described in section II.D.

V. Multibody Model of the Leading Edge of the Wing

The leading-edge, high-lift devices comprise the droop nose and slats 1 to 6 with their support structures (Fig. 1). As represented by the dotted lines, the droop nose is supported by five tracks, slats 1 to 5 by two tracks each, and the outboard slat 6 is supported by three tracks. The leading-edge devices are also actuated by a central shaft system. As it is modeled in the same manner as that of the trailing-edge devices, it is not described here. The droop nose and the slats have different guidance mechanisms as described in the next section.

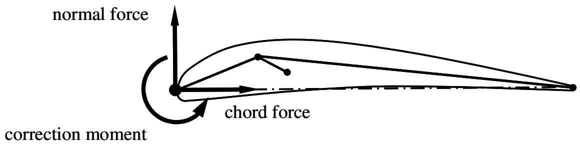

Fig. 10 Application of airloads on the flaps.

A. Droop Nose Guidance Mechanisms

The guidance mechanisms of the droop nose are schematically shown in Fig. 11. The droop nose is supported by five tracks, numbered from 1 to 5. Only tracks 2 and 4 are actuated by means of rotary actuators (active tracks), whereas tracks 1, 3, and 5 are not actuated (passive tracks).

At each track, the droop nose body is supported by the hinge arms AB and the struts CD. The length of struts CD can be changed in order to adjust the position of the droop nose and to achieve a predefined contact pressure between the trailing edge of the droop nose body and the wing structure. The desired aerodynamic effect of the droop nose is only achieved if the gap at the trailing edge of the droop nose is kept closed in all positions.

The points A of all five hinge arms lie on a line called the hinge line, around which the droop nose rotates during extension. At the active tracks 2 and 4, the droop nose is actuated by the rotating lever arms via the drive struts EF. Planetary gearboxes transfer the rotation of the central shaft system of the leading edge into the rotation of the lever arms. The droop nose is supported in spanwise direction by means of the side strut GH. The joints in points A to H are spherical joints to avoid overconstrained mechanisms that would lead to excessive joint forces in the case of elastic deformations of the mechanism components and of the wing structure.

B. Slat Guidance Mechanisms

The slats also perform a rotational motion, whereby the center of rotation is located under the wing for aerodynamic reasons. This requires a different design for the slat guidance mechanisms. The layout for a slat with two tracks is schematically shown in Fig. 12. The slat is supported by two circular racks that are guided by roller pairs in the vertical (main roller) and spanwise (side roller) directions. The rack bears a geared rim in which the drive pinion engages. The

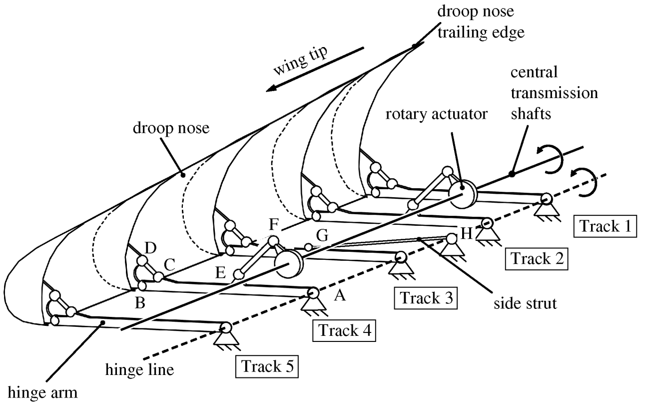

Fig. 11 Droop nose guidance mechanisms.

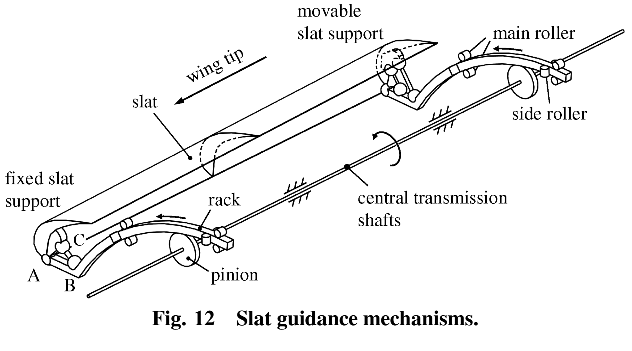

Fig. 12 Slat guidance mechanisms.

pinions are driven by the central transmission system of the leading edge.

The connections between the slat structure and the racks provide a fixed and a movable support in spanwise direction to avoid an overconstrained system. At the fixed support, the rack is connected by a spherical joint and an additional pendular strut with the slat. At the movable support, the single spherical joint is replaced by a linkage consisting of a spherical and a revolute joint, similar to that of Fig. 7a. The elastic droop nose body is modeled in analogy to the flap bodies described in Sec. IV.B.

C. Multibody Modeling of the Leading-Edge Mechanisms

The multibody model of the droop nose mechanisms in Fig. 11 consists of rigid bodies, spherical joints, and universal joints only. The latter are introduced to avoid identical DOF that may lead to numerical problems. As a large bending moment in the hinge arms occurs under airloads, they are modeled by flexible bodies so that the deformation is taken into account.

The multibody model of the slat guidance mechanisms in Fig. 12 is more complex. As the actual contact forces between the rack and the rollers are of interest, the contacts between rack and rollers have to be modeled individually. A single roller behaves like a single-sided constraint for the rack. However, this model is complex, as contact and noncontact situations have to be identified, leading to a structure-variable system. Instead, an approximation of the single-sided constraints by means of specific applied-force laws is realized. The model of the rack with one roller is shown in Fig. 13.

The rack is modeled by using the extrusion element from MSC.Adams. The mass and inertia properties are automatically calculated according to the geometric properties of the rack. A roller is substituted by an auxiliary linkage consisting of two orthogonal prismatic joints and a point-to-curve constraint. The contact force is approximated by a spring with a nonlinear force law that approximates a single-sided constraint (Fig. 14)

$$F = c_N \cdot d^{-\frac{1}{p}} \tag{45}$$

with a stiffness coefficient c_N, and the sliding displacement of the prismatic joint d. The transition to an ideal one-sided constraint is obtained for the exponent $p \to \infty$.

The contact force distribution over the width of the main rollers may be uneven due to elastic or thermal deformations or assembly tolerances. To describe this effect, each main roller is modeled by two substitute mechanisms, as seen in Fig. 12, located side by side in spanwise direction. The arrangement of the rollers in pairs, on opposite sides of the rack, leads to backlash that is adjusted during assembly by appropriate procedures. In the model, a given backlash is described by the definition of the zero points of the force characteristics of the auxiliary mechanisms.

As described in the preceding section, the rack is driven by the pinion. To impress a tangential force between the tooth flanks of rack and pinion, the gear element of MSC.Adams is used. Each of the contacting bodies of the gear element must be born by a revolute joint. As the rack is supported by the rollers, this condition cannot be directly realized. Instead, an auxiliary linkage is used in the MSC.Adams model (Fig. 15). It consists of the link AB rigidly attached to the rack body and the link BC connected with the extended rack body by a revolute joint in B. Another auxiliary link CD is connected with link BC by a universal joint in C and supported by a planar joint in D. The auxiliary linkage supports the reaction force of the pinion in the direction of CD because of the drive torque M, whereas the rack is supported by the rollers only. The rotations of the pinion and the central transmission shafts are linked by a coupler. The elastic slat bodies are modeled in analogy to the flap bodies described in Sec. IV.B.

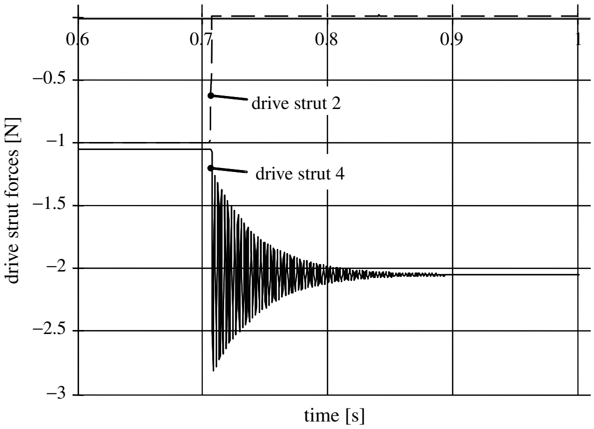

Fig. 14 Contact force model for the rollers.

VI. Simulation Studies

This section first presents simulation results gained from the multibody model. Next, operating and failure load cases of the inboard flap device are investigated. Finally, an operating load case and a failure load case of the droop nose device are shown. It is noted that the numbers of the physical variables are normalized.

A. Simulation Study of the Trailing Edge

The multibody model of the flap mechanism is used for kinematic and dynamic simulation studies. The kinematics of the flap mechanism are characterized by the nonlinear transmission ratio between the rotation angle of the lever arm of the rotary gear actuator and the angle of the flap (Fig. 16).

It is seen that the inboard and outboard flap passes the position of 0 deg twice, with an almost translational motion between. These positions are called 0 deg retracted and 0 deg extended. The 0 deg extended position is used for takeoff because the wing area is

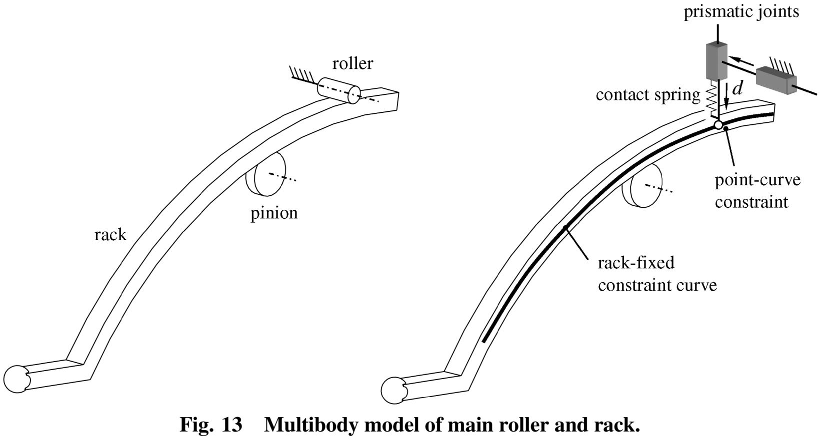

Fig. 13 Multibody model of main roller and rack.

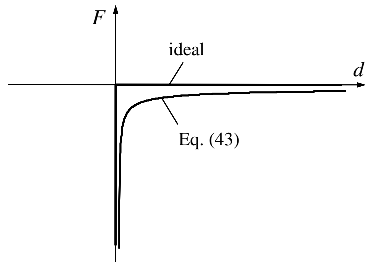

Fig. 15 Auxiliary linkage for the slat mechanism.

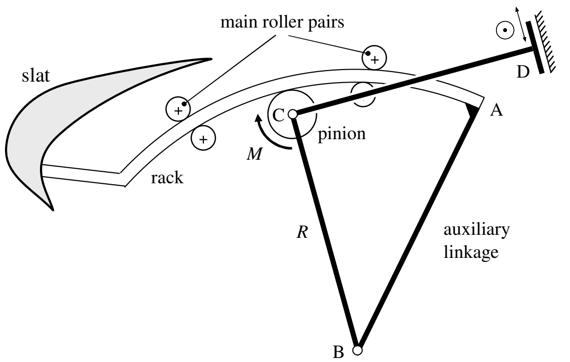

Fig. 16 Angle of flap vs angle of rotary actuator.

increased without raising the aerodynamic drag of the wing. Beyond the 0 deg extended position, the rotational motion of the flap starts.

The relative motion of the flap bodies is also relevant for the design of the flap kinematics. In particular, there are limitations in the relative motion of the flap bodies because of the maximum length of the interconnection strut (see Fig. 9).

The relative motion $\ell(t)$ of the indenter in the casing, during extension of the flaps from their fully retracted position to the fully extended position for a prescribed angular motion of the rotary actuator, is shown in Fig. 17.

Beyond kinematic studies, the dynamics of the flap devices are simulated by the multibody model. An application is the proof of the structural integrity of critical mechanism components under operational and failure conditions. A critical component of the flap devices is the drive strut of track 2, which is loaded by high-compression forces leading to the failure mode of buckling. The drive strut forces of tracks 1 and 2 during extension of the inner flap, under operational airloads in Fig. 18, show that the drive strut of track 2 is loaded by a compression force about four times larger than the tension force in the drive strut of track 1. The different signs of the forces are caused by the arrangement of the drive mechanisms of the tracks before and behind the flap, respectively, as shown in Fig. 5.

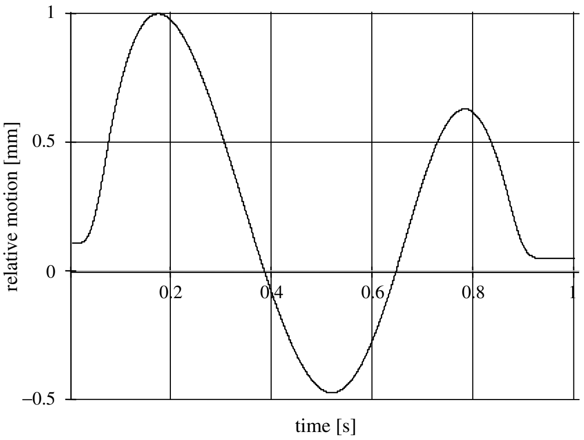

Fig. 18 Drive strut forces of the inboard flap (operational load case).

To prove the fail-safe design of the flap devices, the behavior of the drive strut in the case of buckling is simulated. For this purpose, the drive strut is removed with airloads applied, and the inboard flap has to be supported by the drive strut of track 1 and the interconnection strut between the flaps. For an extension of the flaps under airloads, the drive strut forces of tracks 1 and 2 are shown in Fig. 19 (for a failure of the drive strut of track 2, occurring at about $t = 0.65$ s). To compare the forces of the operational and failure load cases, the same scale factor to normalize the forces is used as in Fig. 18. Although the strut force of track 2 becomes zero, the strut force of track 1 shows a peak value of about the factor six over the value before failure while the strut takes over the load. The stationary value of the strut force of track 1 is still about two times higher than before failure.

After failure, the interconnection strut between the flaps becomes active as an auxiliary load path. In Fig. 20, the motion $\ell(t)$ of the intender relative to the casing, in the operational and failure cases, is compared. It is seen that the interconnection strut is instantaneously compressed at the moment of failure. At the contact of the intender with the end stop of the casing, modeled by a BISTOP element that represents a double-sided impact force element, a short vibration occurs before the stationary value is reached.

The corresponding contact force in the interconnection strut is shown in Fig. 21. Before failure, the interconnection strut force is zero. Compared with the strut force of track 1 in Fig. 19, the peak values of the interconnection strut force immediately after failure have the same order of magnitude, whereas the stationary value is at about the half level.

B. Simulation Study of the Leading Edge

Simulation studies for the leading-edge devices have been performed in the same way as for the trailing-edge devices. The main

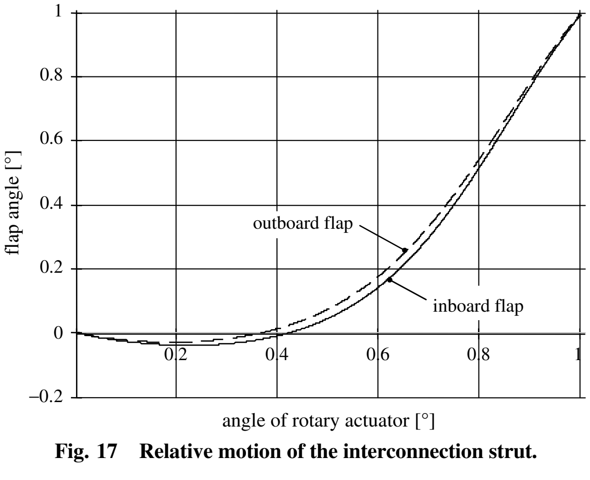

Fig. 17 Relative motion of the interconnection strut.

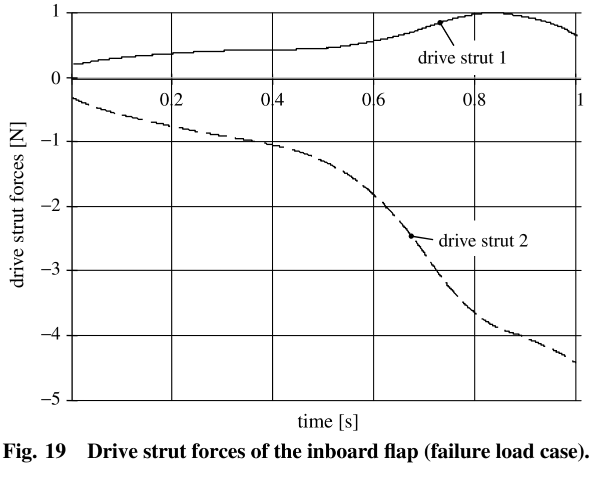

Fig. 19 Drive strut forces of the inboard flap (failure load case).

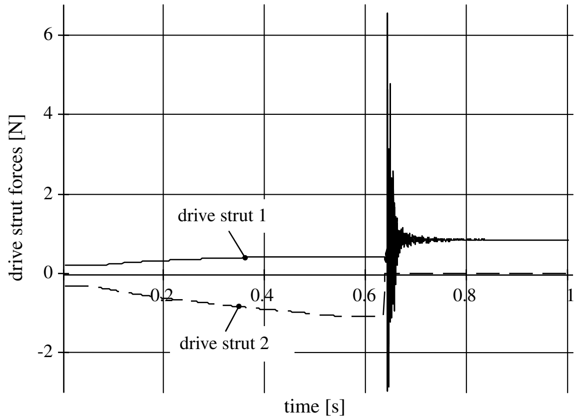

Fig. 20 Relative motion of the interconnection strut (failure load case).

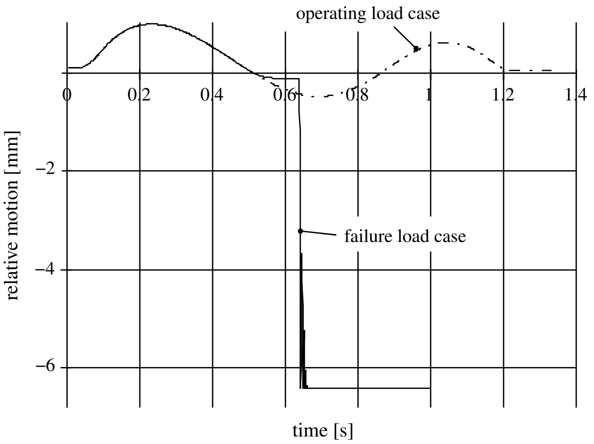

Fig. 21 Contact forces at the interconnection strut (failure load case).

difference between the kinematics of the leading-edge and trailing-edge devices is that the gear ratio between the actuator angle and the device angle is linear for the slats and nearly linear for the droop nose (Fig. 22).

The dashed curve presents the generic linear transmission behavior between the pinion angle and the slat angle. The transmission behavior of the four-bar linkage of the droop nose device (Fig. 11) is not generically linear but achieved by proper definitions of geometric linkage parameters.

In analogy to the trailing-edge investigation described in Sec. VI.A, the collapse of the drive strut of track 2 at the droop nose device is considered (Fig. 11). The spherical joint E of track 2 is deactivated during extension of the droop nose under airloads at about $t = 0.715$ s. The load has to be taken over by the remaining drive strut at track 4 alone, as there is no auxiliary support path. The result for a failure of track 2 in Fig. 23 shows the load transfer to track 4. For a fail-safe design, the drive strut must be dimensioned according to these loads.

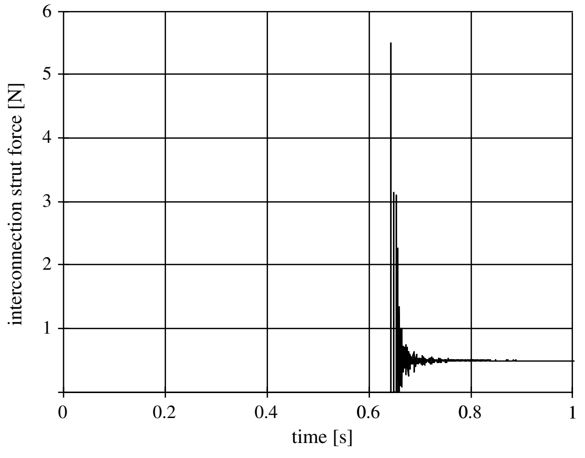

Fig. 22 Kinematics of leading-edge devices.

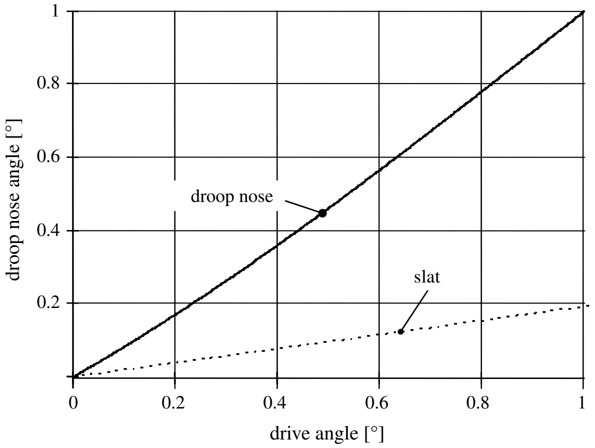

Fig. 23 Drive strut forces of the leading edge (failure load case).

VII. Conclusions

Based on a brief description of the theoretical background, modeling of transport aircraft high-lift mechanisms as elastic multibody systems by using commercial simulation tools has been presented. The parametric model definition allows immediate parameter variations (e.g., optimization with respect to weight, design, space, and aerodynamic efficiency). The multibody models are used in actual high-lift developments. Ongoing work includes an elastic wing structure in order to simulate the behavior of the high-lift devices under more general conditions. Especially in the early design process, multibody simulations allow considerable reductions of development time and costs. Simulations of failure modes can contribute to shortened certification processes. Nevertheless, experiments will be still necessary to validate model uncertainties like friction or damping.

References

[1] Carl, U., High Lift Systems, Europads 2001, Technical Univ. of Hamburg-Harburg, Hamburg, Germany,2001.
[2] Rudolph, P. K. C., “Flap Assembly for Aircraft Wing,”Boeing, Seattle, WA, U.S. Patent No. 4353517, 12 Oct. 1982.
[3] Rudolph, P. K. C., “High-Lift Systems on Commercial Subsonic Airliners,”NASA Ames Research Center, CR 4746, Moffett Field, CA, 1996.
[4] Rudolph, P. K. C., “Mechanical Design of High Lift Systems for High Aspect Ratio Swept Wings,” NASA Ames Research Center, CR 196709, Moffett Field, CA, 1998.
[5] Amirouche, F., *Fundamentals of Multibody Dynamics: Theory and Applications*, Birkhäuser, Boston, 2004.
[6] Nikravesh, P. E., *Planar Multibody Dynamics: Formulation, Programming, and Applications*, CRC Press, Boca Raton, FL, 01 Nov. 2007.
[7] Roberson, R. E., and Schwertassek, R., *Dynamics of Multibody Systems*, Springer, New York, 1988.
[8] Shabana, A. A., *Dynamics of Multibody Systems*, 2nd ed., Cambridge Univ. Press, New York, 1998.
[9] Wilson, C. E., Sadler, J. P., and Michels, W. J., *Kinematics and Dynamics of Machinery*, HarperCollins, New York, 1983.
[10] Wittenburg, J., *Dynamics of Multibody Systems: Dynamics of Systems of Rigid Bodies*, 2nd ed., Springer, New York, 2007.
[11] Schiehlen, W.O., *Advanced Multibody System Dynamics: Simulation and Software Tools*, Kluwer Academic, Norwell, MA, 1993.
[12] Xie, M., *Flexible Multibody System Dynamics: Theory and Applications*, Taylor and Francis, Washington, D.C., 1994.
[13] Zheng, Z.-C., and Xie, G., “A New Approach of the Dynamic Substructure Method”, *Acta Mechanica Solida Sinica*, Vol. 5, No. 4, Oct. 1992, pp. 407–417.

[14] MSC.Adams, Software Package, Ver. 2007r1, MSC Software Corp., Santa Ana, CA.

[15] Meirovitch, L., *Fundamentals of Vibrations*, McGraw–Hill, New York, 2002.

[16] Bathe, K.-J., *Finite Element Procedures*, Prentice–Hall, Upper Saddle River, NJ, 1996.

[17] Zienkiewicz, O. C., and Taylor, R. L.,*The Finite Element Method for Solid and Structural Mechanics*, 6th ed., Elsevier, New York, 2005.

[18] Ewins, D. J., *Modal Testing: Theory, Practice, and Application*, 2nd ed., Research Studies Press, Philadelphia, 2000.

[19] James, M. L., Smith, G. M., Wolford, J. C., and Whaley, P. W., *Vibration of Mechanical and Structural Systems: with Microcomputer Applications*, 2nd ed., HarperCollins, New York, 1989.

[20] Wriggers, P., *Computational Contact Mechanics*, 2nd ed., Springer, Berlin, 2006.